

Forcing mechanisms of the half-precession cycle in the western equatorial Pacific temperature

Received: 11 June 2024

Accepted: 7 February 2025

Published online: 21 February 2025

 Check for updatesZhipeng Wu¹✉, Qiuzhen Yin¹✉, André Berger¹ & Zhengtang Guo²

The western equatorial Pacific (WEP) plays an important role on global climate. Many studies have reported the classical orbital cycles in the WEP temperature variations, but the half-precession (~10-kyr) cycle, despite its uniqueness in the equatorial insolation, is paid less attention. Here, a systematic study on the half-precession cycle in the WEP temperature is performed based on the analysis of transient climate simulations covering the past 800,000 years, combined with high-resolution temperature reconstructions. The results show that the half-precession cycle is a significant signal in the WEP temperature. The model simulations show that in response to astronomical forcing, the half-precession cycle in the WEP surface and upper subsurface temperatures is driven by maximum equatorial insolation, while it is driven by bi-hemisphere maximum insolation in the lower subsurface temperature. The different forcing mechanisms at different depths are related to distinct local ocean circulation patterns. The astronomically-induced half-precession cycles are modulated by eccentricity, CO₂ and ice sheets. Given the importance of WEP on global climate, the half-precession cycle in the WEP temperature may contribute to the half-precession signal recorded in other regions.

The equatorial Pacific plays a critical role in regional and global climate changes. As part of the largest reservoir of warm water on our planet, the western equatorial Pacific (WEP) has a direct effect on the redistribution of heat and moisture over the globe¹, and thus on global climate system, ecosystems, biodiversity, agriculture and the society. The temperature changes in the WEP are often related to large-scale atmospheric circulations (e.g., Hadley and Walker circulations), the Intertropical Convergence Zone (ITCZ), the El Niño-Southern Oscillation (ENSO) and the regional precipitation distribution in the tropics, as well as the climate changes in the mid and high latitudes through atmospheric and oceanic teleconnections^{2–6}. However, the temperature variability in the WEP and its underlying forcing mechanisms are not fully explored largely due to the lack of long-term observations.

The long-term evolution of the WEP temperature in the past could provide insight into a better understanding of the WEP climate

variability and dynamics. Based on proxy reconstructions, striking variations of the WEP temperature on millennial-, orbital- and longer-timescales have been identified^{7–9}. On orbital timescale (tens to hundreds of thousands of years), the reconstructed variations of both the sea surface temperature (SST) and subsurface sea temperature (subT) in the WEP during the Quaternary show clear ~100-kyr glacial-interglacial cycles as well as ~20-kyr and ~40-kyr cycles that could be related to precession and obliquity, respectively^{8,10–18}.

In addition to the slower variations that are characterized by the ~100-kyr, ~40-kyr and ~20-kyr cycles, higher-frequency oscillations that are characterized by the half-precession cycle (~10-kyr) have also been reported in a recent temperature record from the WEP¹⁹. This is quite intriguing. The half-precession cycle is a unique feature in the equatorial insolation, and it could play an important role in the high-low latitude climate interactions and in linking the climate variations on

¹Earth and Climate Research Center, Earth and Life Institute, Université catholique de Louvain, Louvain-la-Neuve, Belgium. ²State Key Laboratory of Lithospheric and Environmental Coevolution, Institute of Geology and Geophysics, Chinese Academy of Sciences, Beijing, China.

✉ e-mail: zhipeng.wu@uclouvain.be; qiuzhen.yin@uclouvain.be

longer orbital timescale and those on millennial timescale. It has been found to be closely linked with known climate events and transitions in the Quaternary, like the Dansgaard-Oeschger events²⁰ and the mid-Pleistocene transition^{21,22}.

Near the Equator, the Sun is in zenith twice a year at each latitude so that the equatorial latitudes receive maximum insolation twice during one precession cycle. This leads to a half-precession cycle in the long-term variations of the maximum equatorial insolation^{23,24}. As a result, it would be expected to observe half-precession cycles in the equatorial temperature variations as a direct response to maximum equatorial insolation^{25,26}. However, among many published WEP temperature reconstructions, the study of ref. 19 is so far the only that explicitly reported the existence of the half-precession cycle in the long-term variations of the WEP temperature reconstruction. Moreover, based on the comparison of their results with the maximum of November meridional insolation gradient between 0° and 30°N and May meridional insolation gradient between 0° and 30°S, the authors suggested that the half-precession signal in the thermocline temperature in the WEP resulted from the interplay of antiphased meridional insolation gradient in the two hemispheres. Indeed, in addition to the maximum equatorial insolation, the variations of the bi-hemisphere maximum insolation and the bi-hemisphere maximum meridional insolation gradient also contain the half-precession cycle^{19,27}.

Therefore, whether there is half-precession signal in the temperature changes in the WEP and what is the forcing mechanism remain uncertain. In addition to high-resolution proxy reconstructions, transient climate simulations are essential for answering these questions. In this study, based on three transient climate simulations covering the past 800 ka (Supplementary Figs. 1, 2) and analysis of high-resolution WEP temperature reconstructions of five cores (KX21-2, MD05-2925, MD06-3067, GeoB17426-3 and MD10-3340, Supplementary Fig. 3), we aim to investigate whether there is half-precession signal in the temperature changes in the WEP and what is its relationship with insolation and how the astronomically-induced half-precession cycle would be modified by the effects of greenhouse gases (GHG) and ice sheets.

Results and discussion

Half-precession cycles in the WEP temperature reconstructions

Figure 1 and Supplementary Fig. 4 show the variations of SST and subT of five cores in the WEP and their power spectra (see Methods). In addition to the -100-kyr, -40-kyr and -20-kyr cycles, these reconstructions also contain significant half-precession (-10-kyr) cycle which reaches at least the 90% significance level, although its power is weaker than the three long cycles. The results of continuous wavelet transform confirm the existence of the half-precession cycle in these WEP temperature reconstructions although it varies in time (Supplementary Fig. 5). To better investigate the half-precession signal, the lower-frequency orbital signals are removed using the high-pass filtering (<15 kyr) (see “Methods”). The results show that the half-precession cycle is strong and clear among the sub-orbital signals (Supplementary Figs. 6, 7), which confirms the reliability of the half-precession cycle in these WEP temperature records. Supplementary Figs. 6, 7 also show that the amplitude of the half-precession cycle in these records varies in time. For instance, in core KX21-2, it is larger before -200 ka BP than after (Supplementary Fig. 6a, b), while in core MD05-2925, it is larger after -300 ka BP than before (Supplementary Fig. 6c, d). The change of the amplitude of the half-precession cycles in time and in different locations could reflect the modulation of temporal and local driving factors on the half-precession cycles. The half-precession cycle is significant in both the SST and subT across these five cores. However, it might not be the case for all available cores in the WEP. For example, in core MD01-2386, the half-precession cycle is found to be significant only in the subT but not in the SST¹⁹, which could reflect local influence.

To investigate the relationship of the half-precession cycles in the WEP temperature reconstructions with insolation, they are compared with the three insolation indexes as mentioned above. It shows that the half-precession cycles in both SST and subT in the five cores have no stable phase relationship with any of the three insolation indexes (Supplementary Figs. 8, 9). This is further confirmed by the cross-wavelet spectra results (Supplementary Figs. 10, 11). Moreover, the half-precession cycles in the SST and subT between the different cores neither have stable phase relationship (Supplementary Figs. 8, 9). It is unclear to which extent the unstable phase relationship between the five cores and between them and insolation is affected by age uncertainties of the cores and/or by local influence. As a result, it is also hard to distinguish which insolation index is responsible for the half-precession cycles in the WEP temperature only based on proxy records. Climate model simulations are needed.

Half-precession cycles in the simulated WEP temperatures

In the analysis of the model results, to avoid possible local impact as for example observed in the five selected cores, we choose the region (10°S–10°N, 120°E–180°E, purple rectangle in Supplementary Fig. 3) to represent the WEP region and the mean climate over this region is analyzed. In addition to SST, ocean temperature at different depths have been analyzed, and the results of three depths at 65 (sub₆₅T), 122 (sub₁₂₂T) and 163 m (sub₁₆₃T) are presented in this paper to represent the upper, transitional and lower subsurface waters, respectively (see Methods).

Figure 2a, b and Supplementary Fig. 12a, b show that under the influence of astronomical forcing alone (Orb experiment), the variations of both SST and sub₆₅T show strong -100-kyr, -40-kyr and -20-kyr cycles, which are related to the eccentricity, obliquity and precession cycles. Moreover, they also contain half-precession cycle (-10-kyr) which has an equivalently strong power as the other long orbital cycles. The strong half-precession cycle in the SST and sub₆₅T also leads to strong half-precession signal in the ocean heat content (OHC) of the upper subsurface water (Supplementary Fig. 13). However, in sub₁₂₂T the half-precession and -100-kyr cycles nearly vanish and their spectra peaks are not statistically significant, leaving only the -40-kyr and -20-kyr cycles (Fig. 2c and Supplementary Fig. 12c). Conspicuously, the half-precession and -100-kyr cycles reemerge in sub₁₆₃T, although they are weaker than the -40-kyr and -20-kyr cycles (Fig. 2d and Supplementary Figs. 12d, 14). Therefore, under the insolation forcing alone, not only are the major cycles related to eccentricity (the -400-kyr cycle of eccentricity is not considered here due to the insufficient length of simulation), obliquity and precession able to be reproduced in our model but also the shorter half-precession cycle that has been identified as a unique feature in the tropical insolation^{23,24}. Figure 2 also indicates that the -100-kyr cycle is strongly linked with the half-precession cycle. This relationship was also observed in the tropical insolation²⁴ and in proxy records²². Another interesting feature emerging from our model results is that in response to insolation alone, strong -100-kyr and -40-kyr cycles could be generated in the WEP temperatures although precession is often considered as the main forcing for low latitude climate.

It is also intriguing that the half-precession cycle is significant in the SST, sub₆₅T and sub₁₆₃T but not in the sub₁₂₂T. Figure 3d, e shows that the half-precession cycles in both the SST and sub₆₅T have a very strong positive correlation with the maximum equatorial insolation. A higher maximum equatorial insolation leads to higher SST and sub₆₅T in the half-precession band. Their positive correlation and in-phase relationship are confirmed by cross-wavelet analysis (Fig. 3g, h). In contrast, the half-precession cycle in the sub₁₆₃T has a strong positive correlation and in-phase relationship with the bi-hemisphere maximum insolation (Fig. 3f, i). A higher bi-hemisphere maximum insolation leads to higher sub₁₆₃T in the half-precession band. These indicate that the half-precession signals in the SST and sub₆₅T result from the

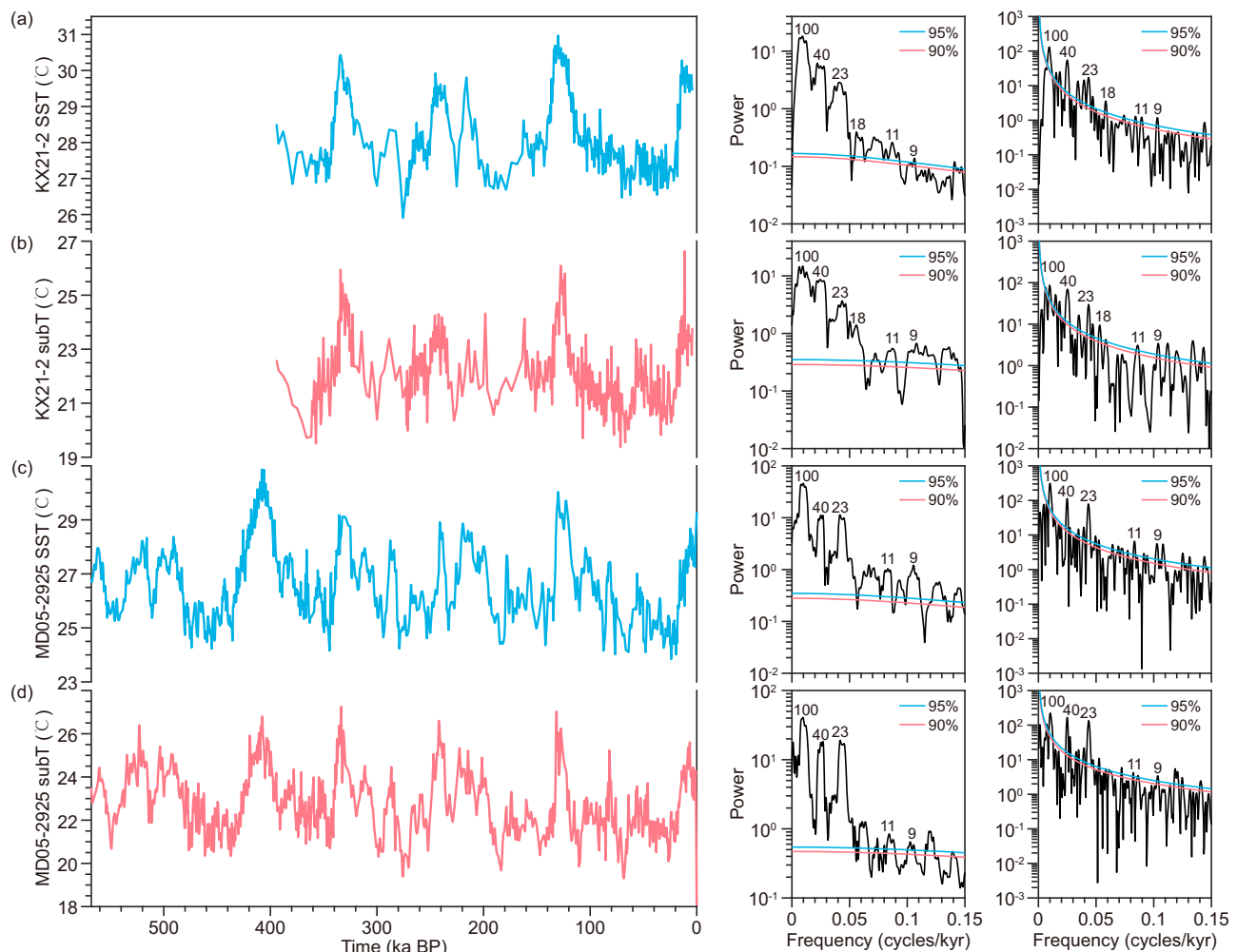


Fig. 1 | Variations of sea surface temperature (SST) and subsurface sea temperature (subT) in the cores KX21-2¹⁵ and MD05-2529¹⁶ (left) and their power spectra using the multi-taper method (mid) and periodogram (right). a SST and

(b) subT in the core KX21-2, c SST and (d) subT in the core MD05-2925. In the power spectra, the pink and blue curves indicate the 90% and 95% significance levels.

maximum equatorial insolation, but it results from the bi-hemisphere maximum insolation in the sub₁₆₃T. In both cases, the amplitude of the half-precession cycle is modulated by eccentricity.

To understand why the half-precession cycle in the WEP SST/sub₆₅T and that in the sub₁₆₃T result from different insolation drivers and why the half-precession cycle nearly disappears in the sub₁₂₂T, the regional ocean circulation patterns at different depths are analyzed. Figure 4a shows that at the 163-m depth, the WEP waters are transported from the subtropics of both northern (NH) and southern hemispheres (SH) toward the Equator via the western boundary path (WBP). Therefore, the temperature at 163 m is strongly linked with the oceanic heat transported from the subtropics of both hemispheres which is in turn linked with the insolation of each hemisphere. This explains why the half-precession cycle in sub₁₆₃T is driven by bi-hemisphere maximum insolation. In contrast, at the surface and the 65-m depth which share similar ocean circulation patterns (Fig. 4c, d), the WEP waters are transported from the tropics to the subtropics of the NH via the Kuroshio Current and to the subtropics of the SH via the East Australian Current. Therefore, at the surface and 65-m depth, the WEP temperature change would be more a driver than a follower of the subtropical Pacific temperatures in both hemispheres, and it responds more directly to equatorial insolation. This explains why the half-precession cycles in the SST and sub₆₅T are driven by maximum equatorial insolation instead of by bi-hemisphere maximum insolation.

The 122-m depth is at the transition between the upper and lower subsurface waters and has therefore different ocean circulation pattern (Fig. 4b). At this depth, the WBP in the SH is hardly seen, leading to a much weaker influence of the SH subtropical waters on the WEP as compared to the 163-m depth and therefore a much weaker impact of the SH insolation. This explains the insignificant half-precession cycle in the sub₁₂₂T.

Although the half-precession cycle in both SST and sub₆₅T is driven by maximum equatorial insolation, we can also notice that the amplitude of the half-precession cycle is slightly smaller in SST than in sub₆₅T (Fig. 2a, b). This could be attributed to precipitation feedback. While higher maximum equatorial insolation increases WEP SST and sub₆₅T, it also leads to more precipitation in the WEP (Supplementary Fig. 15), which in turn dampens SST variability. The weaker half-precession cycle in sub₁₆₃T as compared to the ~20 kyr and ~40 kyr cycles, could be explained by that the WBP in the NH subtropics is stronger than that of the SH, leading to a dominant effect from the NH (Fig. 4a) and therefore a weaker half-precession signal.

Effects of GHG and ice sheets on the half-precession cycle

When the effect of GHG is added on the effect of insolation (OrbGHG experiment), the ~100-kyr cycle in the SST and sub₆₅T is strongly enhanced and becomes the dominant cycle, showing the strong effect of CO₂ on the SST and sub₆₅T (Fig. 5a, b). The dominant role of CO₂ in

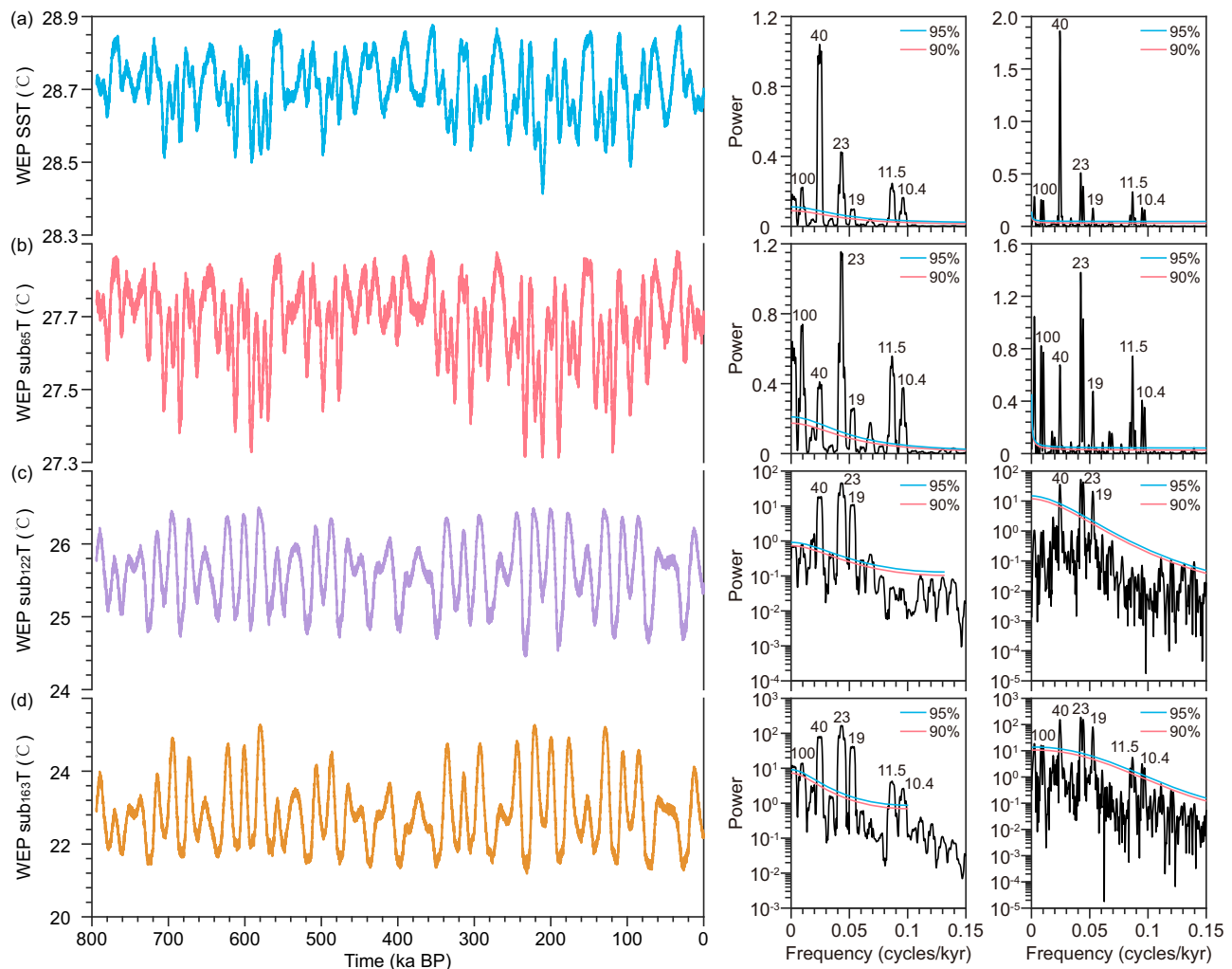


Fig. 2 | Simulated variations of the western equatorial Pacific (WEP) temperature over the past 800 ka in the Orb experiment (left) and their power spectra using the multi-taper method (mid) and periodogram (right). a sea surface temperature (SST), subsurface sea temperature at **(b)** 65 (sub₆₅T), **(c)** 122 (sub₁₂₂T)

and **(d)** 163 m (sub₁₆₃T). A 100-year mean is performed on the curves of SST, sub₆₅T, sub₁₂₂T and sub₁₆₃T variations to reduce the high-frequency fluctuations. In the power spectra, the pink and blue curves indicate the 90% and 95% significance levels. Source data are provided as a Source Data file.

the SST aligns with the results of proxy records and an ice-sheet climate coupled model^{8,10}. In contrast, the effect of CO₂ on the sub₁₂₂T and sub₁₆₃T is relatively minor, leaving them primarily influenced by the ~20-kyr cycle and followed by the ~40-kyr cycle, as observed in the Orb experiment (Fig. 5c, d). The dominant ~20-kyr cycle in the sub₁₂₂T and sub₁₆₃T is consistent with the subsurface temperature records¹⁵.

The half-precession cycle is still clearly present in the SST and sub₆₅T (Fig. 5a, b), although its strength is reduced as compared to the Orb simulation and it is weaker than the other three longer cycles due to the influence of these long cycles in the GHG concentration. The half-precession signal in the SST and sub₆₅T in the OrbGHG simulation still has a positive and in-phase relationship with the maximum equatorial insolation (Fig. 6c, f and Supplementary Fig. 16c, f), although the relationship is not as perfect as in the Orb simulation. This shows that the effect of GHG does not principally alter the phase of the insolation-induced half-precession cycles in the SST and sub₆₅T. However, it can also be noted that GHG can modulate this phase relationship especially during the time periods when eccentricity is small, such as ~800–700 ka BP and the last 100 ka. During these periods, the half-precession cycles are relatively weak due to weak variation of precession caused by small eccentricity²⁸, and are therefore subject to the influence of GHG which can shift the timing of the peaks of the half-precession cycle in the SST and sub₆₅T. The effect of GHG also modulates the

amplitude of variations of the half-precession cycles in the SST and sub₆₅T (Fig. 6c and Supplementary Fig. 16c), but the effect of eccentricity on the amplitude modulation can still be clearly seen. Given the weak effect of GHG on the sub₁₆₃T, the half-precession cycle remains clearly evident in the sub₁₆₃T in the OrbGHG experiment, with a strength comparable to that in the Orb experiment (Fig. 5d). It still has an in-phase relationship with the bi-hemisphere maximum insolation (Supplementary Fig. 17c, f).

From the OrbGHG to the OrbGHGIce simulations, there is no fundamental change in the variations of the SST, sub₆₅T, sub₁₂₂T and sub₁₆₃T nor in their spectra (Fig. 5). This is because the NH ice sheets have a much weaker effect on the SST and sub₆₅T than GHG, and have a much weaker effect on the sub₁₂₂T and sub₁₆₃T than insolation. Due to the additional influence of the ~100-kyr cycle in the NH ice volume, the ~100-kyr cycle in the SST, sub₆₅T, sub₁₂₂T and sub₁₆₃T variations is slightly stronger in the OrbGHGIce than in the OrbGHG simulation (Fig. 5).

In the OrbGHGIce simulation, the half-precession cycle remains evident in the SST and sub₆₅T (Fig. 5a, b), and the effect of NH ice sheets on the half-precession cycle is weaker as compared to GHG (Fig. 6d and Supplementary Fig. 16d). The phase of the half-precession cycle in the SST/sub₆₅T with maximum equatorial insolation is further altered, leading to less stable phase relationship than in the Orb simulation (Fig. 6g and Supplementary Fig. 16g). The half-precession

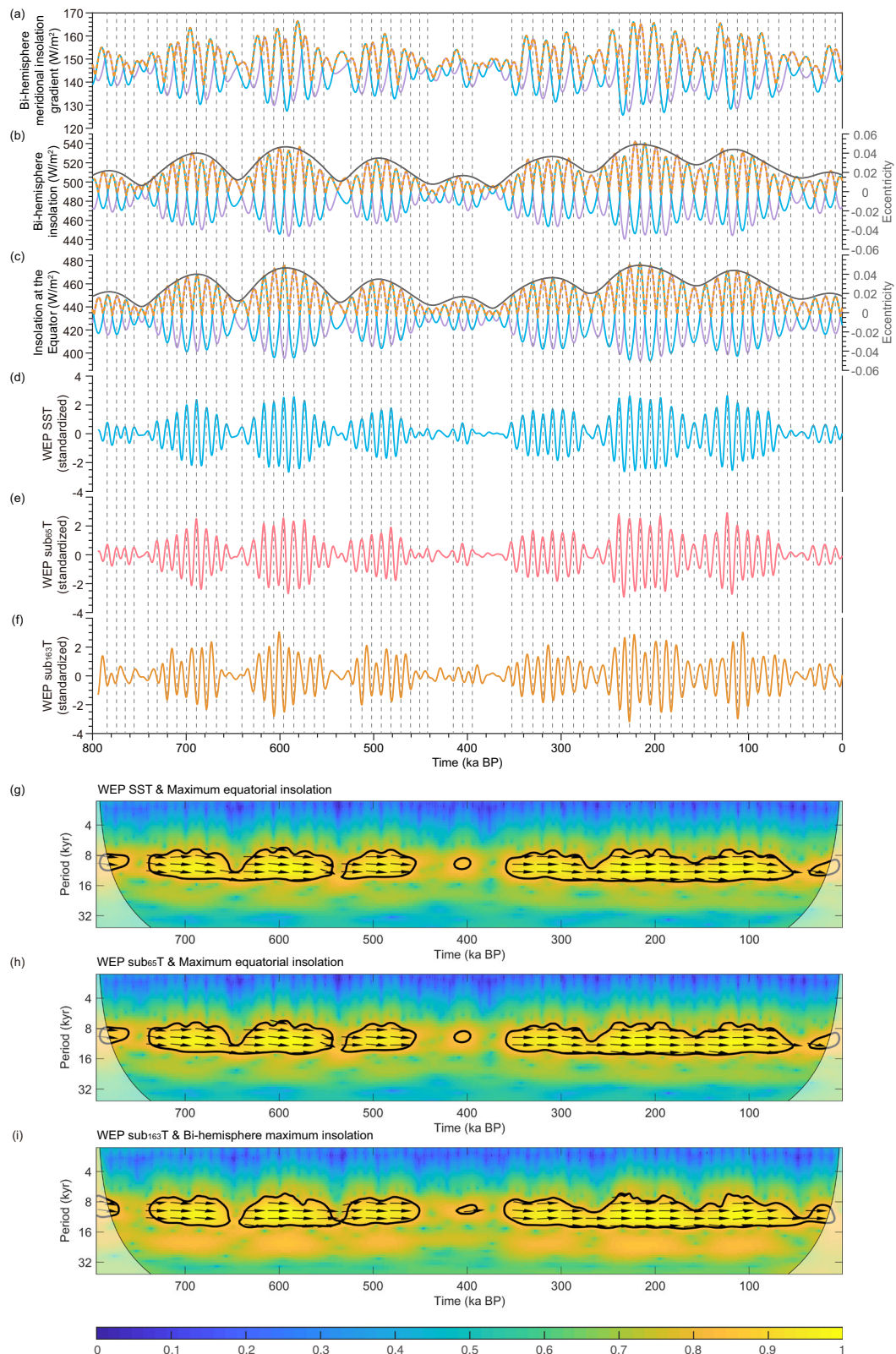


Fig. 3 | Comparison of the half-precession cycles in the western equatorial Pacific (WEP) sea surface temperature (SST), subsurface sea temperature at 65 (sub₆₅T) and 163 m (sub₁₆₃T) variations in the Orb simulation with the three insolation indexes. **a Bi-hemisphere meridional insolation gradient: the purple (blue) line is November (May) meridional insolation gradients between 0° and 30°N (between 0° and 30°S), and the yellow dashed line is the maximum of them⁴⁰. **b** Bi-hemisphere insolation: the purple (blue) line is June (December) insolation at 30°N (30°S), and the yellow dashed line is the maximum of them⁴⁰. The gray line is**

eccentricity. **c** Insolation at the Equator: the purple (blue) line is March (September) insolation, the yellow dashed line is the maximum of them⁴⁰. The gray line is eccentricity. **d–f** The filtered half-precession cycle (8–12 kyr) of SST, sub₆₅T and sub₁₆₃T, respectively. The vertical dashed lines indicate the peaks of the half-precession cycle of SST. **g** Cross wavelet spectra between the SST and the maximum equatorial insolation. **h** Same as **(g)**, but for sub₆₅T. **i** Cross wavelet spectra between the sub₁₆₃T and the bi-hemisphere maximum insolation.

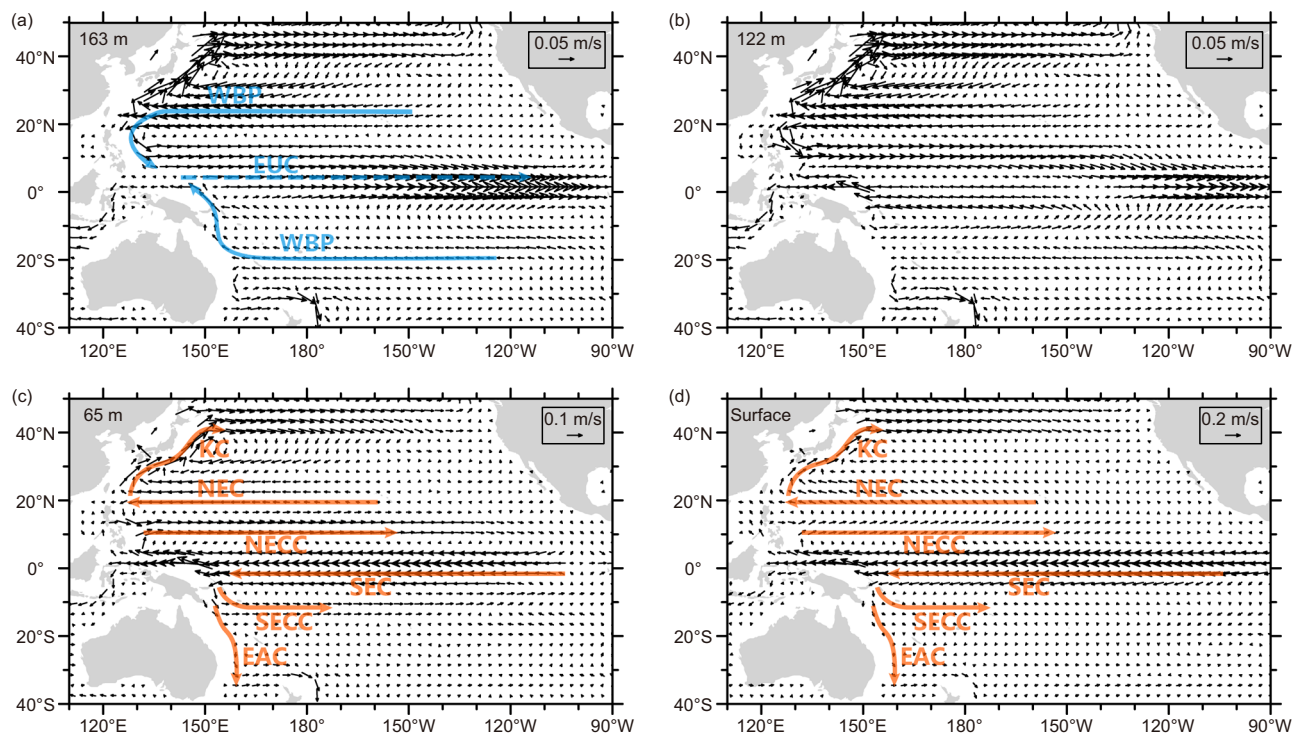


Fig. 4 | Simulated mean annual ocean circulation over the past 800 ka in the Orb simulation. Ocean circulation at the depths of (a) 163, (b) 122, (c) 65 m and (d) the surface. The major currents are indicated: KC Kuroshio Current, NEC North Equatorial Current, NECC North Equatorial Counter Current, SEC South Equatorial Current, SECC South Equatorial Counter Current, EAC East Australian Current, WBP Western Boundary Path, EUC Equatorial Undercurrent. Source data are provided as a Source Data file.

Current, SECC South Equatorial Counter Current, EAC East Australian Current, WBP Western Boundary Path, EUC Equatorial Undercurrent. Source data are provided as a Source Data file.

cycle is also clearly present in the $sub_{163}T$, showing a power similar to that in the Orb experiment (Fig. 5d). This is because the effect of NH ice sheets on the $sub_{163}T$ is weaker as compared to insolation. Furthermore, it maintains a relatively stable phase relationship with the bi-hemisphere maximum insolation, and its amplitude is still modulated by eccentricity (Supplementary Fig. 17d, g).

In summary, our study reveals that the half-precession cycle emerges as a significant signal in many WEP temperature reconstructions and in our simulated WEP temperature. Our model simulations show that under the astronomical forcing alone, strong half-precession cycle can be simulated in the WEP surface and upper subsurface ocean temperature and it is driven by maximum equatorial insolation. Weaker but significant half-precession cycle can also be simulated in the lower subsurface ocean temperature, but it is driven by bi-hemisphere maximum insolation. No significant half-precession cycle is simulated in the ocean temperature in the transitional depth. The different characteristics of the half-precession cycle in different ocean depths and the forcing mechanisms are strongly linked to the local ocean circulations. Our simulations also show that the amplitude of the half-precession cycle and its phase relationship with insolation could be modulated by GHG and ice sheets.

The strong half-precession cycle in the surface and upper subsurface ocean temperature in the WEP leads to strong half-precession cycle in the OHC of the upper subsurface water. As both the present-day observations and proxy records suggest that the temperature and upper OHC in the WEP have a great effect on the ENSO variability and the East Asian monsoon^{15,19,29}, the half-precession cycles found in our results could contribute to the explanation of the half-precession signals observed in proxy records of ENSO³⁰ and East Asian monsoon^{31,32}. Similarly, the dominant role of CO_2 on the WEP SST and upper subsurface temperature on orbital timescale found in our study could contribute to the explanation of the ~100-kyr cycle observed in the East Asian summer monsoon precipitation^{33–35}.

Methods

Selected WEP temperature reconstructions

In this study, previously published WEP temperature reconstructions of five cores, KX21-2¹⁵, MD05-2925¹⁶, MD06-3067^{13,36}, GeoB17426-3¹³ and MD10-3340¹⁵ (Supplementary Fig. 3), are used to test whether there is a half-precession signal in the temperature changes in the WEP. These reconstructions have a relatively high resolution (<1 ka) and long duration (>150 kyr), and each of them contains both SST and subT reconstructions. The age models of the five cores are established by accelerator mass spectrometry radiocarbon (AMS ^{14}C) dates and the correlation of their benthic foraminifera $\delta^{18}O$ with the global stacked benthic foraminifera $\delta^{18}O$ (LR04 stack)³⁷. The average temporal resolution of cores KX21-2¹⁵, MD05-2925¹⁶, MD06-3067^{13,36}, GeoB17426-3¹³ and MD10-3340¹⁵ are about ~900, ~570, ~390, ~850 and ~360 years respectively. The SST and subT of the five cores are reconstructed based on the Mg/Ca ratios of the surface dweller *Globigerinoides ruber* and the subsurface dweller *Pulleniatina obliquiloculata* respectively. These SST and subT records were not used to discuss the half-precession cycle in their original publications although some performed spectral analysis. More information about the SST and subT reconstructions of these five cores can be found in their original publications^{13,15,16,36}.

Climate model and simulations

The model used in this study is LOVECLIM1.3, a three-dimension Earth system Model of Intermediate Complexity (EMIC)³⁸. The model setup is the same as the one used in the previous study³⁹. In our study, the atmosphere (ECBilt), the ocean and sea ice (CLIO) and the terrestrial biosphere (VECODE) are interactively coupled. ECBilt is a spectral atmospheric model with a horizontal T21 truncation, which corresponds approximately to a horizontal resolution of $5.625^\circ \times 5.625^\circ$. It has three vertical layers and its dynamics are governed by the quasi-geostrophic potential vorticity. VECODE is a two-dimensional

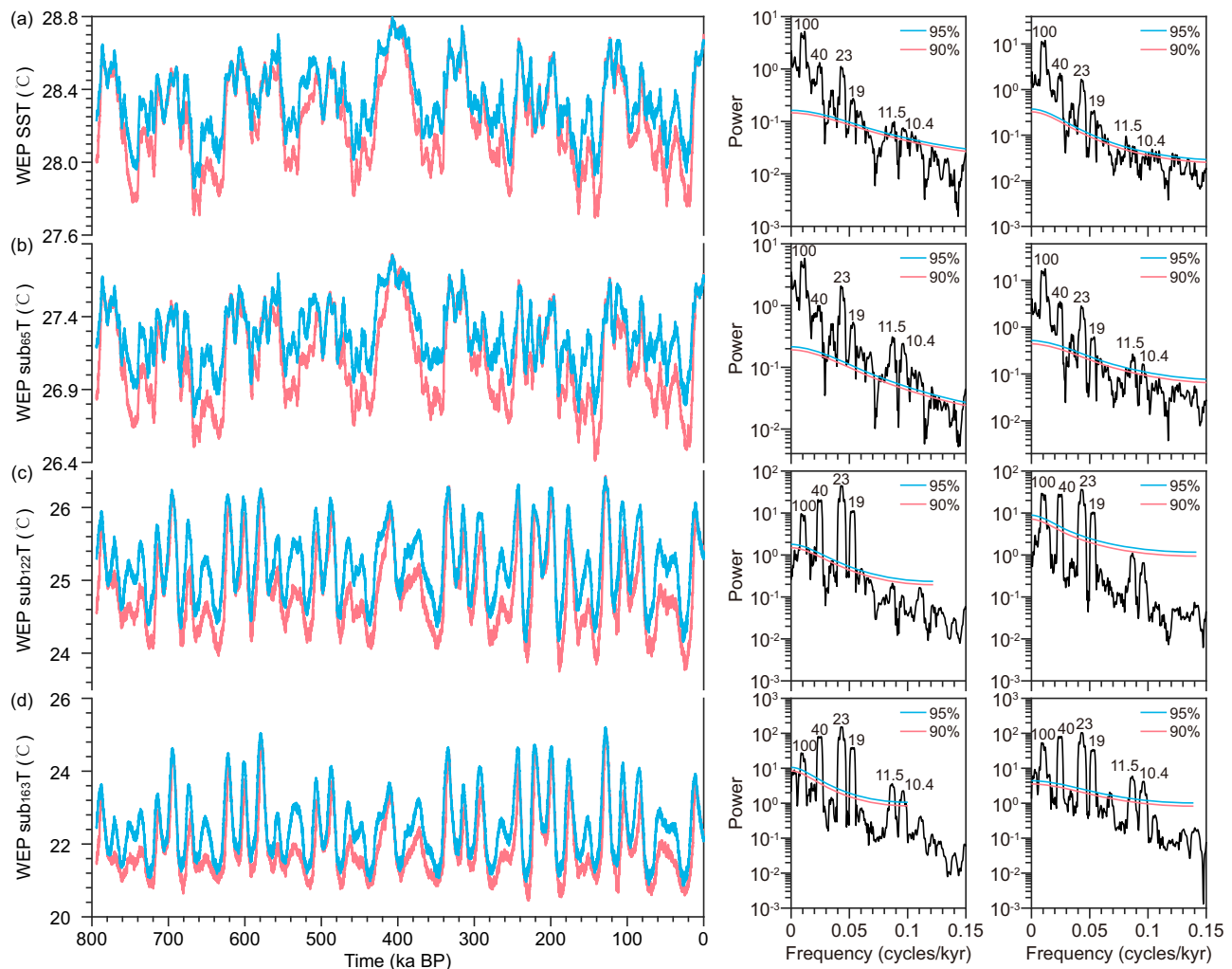


Fig. 5 | Simulated variations of the western equatorial Pacific (WEP) temperature over the past 800 ka in the OrbGHG (blue curves) and OrbGHGIce (pink curves) experiments (left), and their power spectra using the multi-taper method (mid is for OrbGHG experiment and right is for OrbGHGIce experiment). a sea surface temperature (SST), subsurface sea temperature at **(b)** 65

(sub₆₅T), c 122 (sub₁₂₂T) and **(d)** 163 m (sub₁₆₃T). A 100-year mean is performed on the curves of SST, sub₆₅T, sub₁₂₂T and sub₁₆₃T variations to reduce the high-frequency fluctuations. In the power spectra, the pink and blue curves indicate the 90% and 95% significance levels. Source data are provided as a Source Data file.

dynamical terrestrial vegetation model including two plant functional types: tree and grass, and its resolution is the same as ECBilt. CLIO is a global free-surface ocean general circulation model coupled to a thermodynamic-dynamic sea ice model. The horizontal resolution of CLIO is 3° in longitude and latitude, and there are 20 unevenly spaced vertical layers in the ocean. For example, layers 1–10 correspond to the depth 0–10 m, 10–22 m, 22–36 m, 36–54 m, 54–76 m, 76–104 m, 104–139 m, 139–187 m, 187–253 m and 253–346 m. In addition to SST, the ocean temperatures of layers 5, 7 and 8 are presented in this study to represent the upper, transitional and lower subsurface waters, respectively, which correspond to the subsurface waters of the depths 10–104 m, 104–139 m, and below 139 m. These depths are defined according to their distinct local ocean circulation patterns and different characteristics of the half-precession cycle, and also considering the vertical resolution of our ocean model. Layer 1 is the surface, and 65, 122 and 163 m are the mean depth of layers 5, 7 and 8 respectively.

To make a comprehensive and systematic investigation of the half-precession cycle in the WEP temperature during glacial-interglacial cycles, we have performed transient simulations covering the past 800 ka driven by orbital forcing, GHG and NH ice sheets (Supplementary Fig. 1). Although LOVECLIM3 is classified as an EMIC model, its complexity is high for this kind of models and its ocean

component is a full general circulation model. As a result, it is hard to use LOVECLIM3 to directly perform one single transient simulation going from 800 ka BP to the present. Therefore, we split the simulation into nine segments and run them in parallel, with an overlap of 5 ka between each segment (Supplementary Fig. 2).

Three transient simulations are performed for each segment. To avoid any possible impact of acceleration on sub-orbital scale climate variations and the oceanic climate, no acceleration is used in our simulations. The first two simulations, Orb and OrbGHG, were performed in the previous study³⁹. In the Orb simulation, to investigate the effect of insolation alone, only the astronomical parameters⁴⁰ vary with time, the GHG concentrations and ice sheets being fixed to their pre-industrial conditions. The initial condition of each segment is provided by a 2000-year equilibrium experiment with the pre-industrial GHG and ice sheets, and astronomical parameters at the starting date of the simulated period. In the OrbGHG simulation, both the GHG concentrations^{41–43} and astronomical parameters vary with time, the ice sheets being fixed to their pre-industrial conditions. The initial condition of each segment is provided by a 2000-year equilibrium experiment with the pre-industrial ice sheets, and GHG and astronomical parameters at the starting date of the simulated period. The effect of GHG can be investigated by comparing the OrbGHG simulation with the

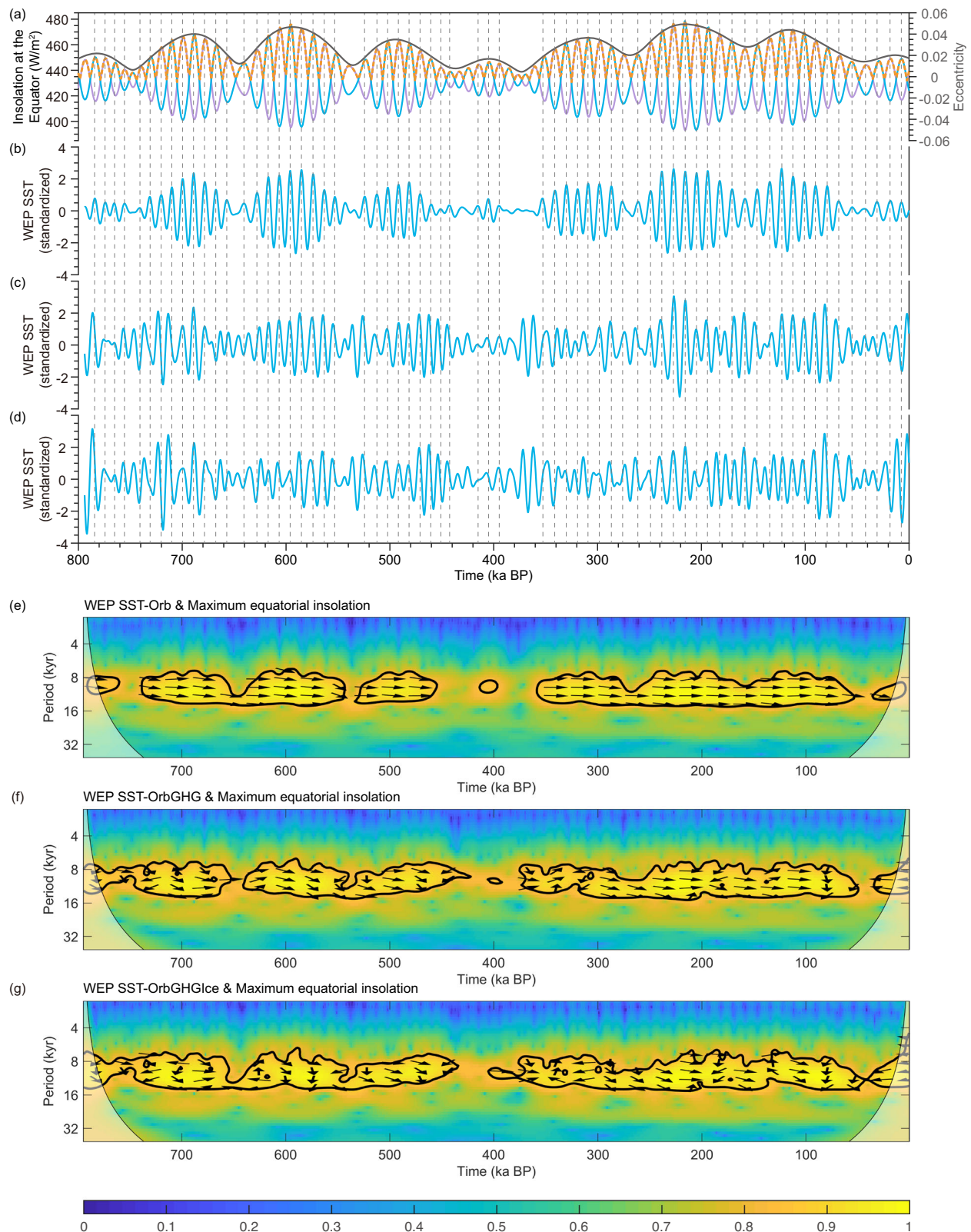


Fig. 6 | Comparison of the half-precession cycles in the western equatorial Pacific (WEP) sea surface temperature (SST) variations in the three simulations with the maximum equatorial insolation. **a** Insolation at the Equator: the purple (blue) line is March (September) insolation, the yellow dashed line is the maximum of them⁴⁰. The gray line is eccentricity. **b–d** The filtered half-precession cycle

(8–12 kyr) of SST in the Orb, OrbGHG and OrbGHGIce simulations, respectively. The vertical dashed lines indicate the peaks of the half-precession cycle of SST in the Orb simulation. **e–g** Cross-wavelet spectra between the SST of the three simulations and the maximum equatorial insolation.

Orb simulation. In the third simulation, OrbGHGIce, the NH ice sheets⁴⁴, GHG concentrations and astronomical parameters all vary with time, and the Southern Hemisphere ice sheets are fixed to the pre-industrial condition. The initial conditions were provided by a 2000-year equilibrium experiment with the NH ice sheets, GHG concentrations and astronomical parameters at the starting date of the simulated period. In the presence of land ice, albedo, topography, vegetation and surface soil types corresponding to ice-covered condition were prescribed at corresponding model grids in LOVECLIM1.3⁴⁵. The effect of NH ice sheets can be investigated by comparing the OrbGHGIce simulation with the OrbGHG simulation. We finally obtain three continuous transient simulations covering the entire past 800 ka by concatenating the data from each segment and by applying a time-sliding linear interpolation for the overlap periods. This allows us to investigate the respective impact of astronomical forcing, CO₂ and ice sheets on the half-precession cycle in the WEP temperature.

Time series analysis

To investigate the half-precession cycles in the WEP temperature reconstructions and in our transient climate simulations, time series analysis is performed, including power spectra, continuous wavelet transform and cross-wavelet spectra. The original temperature reconstructions are linearly interpolated into an even time step of 500 years and a 100-year mean is applied on our simulated WEP temperatures before performing the time series analysis.

Power spectra analysis is conducted on both the temperature reconstructions and climate simulations using the Acycle v2.8 software and follows typical procedures⁴⁶. Two different methods, multi-taper method (MTM) and periodogram, are used to test and verify the half-precession cycles in the temperature reconstructions and climate simulations. The time-bandwidth product is set to 2, the zeropadding is set to 5 times of the total length of data and the robust AR(1) red noise is applied when the MTM is performed; the zeropadding is set to 5 times of the total length of data and the Power Law red noise is applied when the periodogram is performed. The 90% and 95% significance levels against red noise are indicated in the power spectra. The Acycle software and its user's guide can be obtained at: <https://acycle.org/>.

Continuous wavelet transform is also performed on the temperature reconstructions and climate simulations to verify the half-precession cycle. Given the strong orbital signals in the temperature reconstructions, the orbital signals (periodicity: >15 kyr, frequency: <0.067 cycles/kyr) are removed using the Matlab's built-in "highpass" function to better investigate the sub-orbital signals. In addition, the half-precession cycles (periodicity: 8–12 kyr, frequency: 0.083–0.125 cycles/kyr) in the temperature reconstructions and climate simulations are extracted using the Matlab's built-in "bandpass" function. The extracted half-precession signals are also compared with the results obtained after the orbital signals are removed, to further test the reliability of the half-precession signals. Moreover, in order to investigate the relationship of the half-precession cycles with insolation, they are compared with three different insolation indexes as proposed by previous studies: maximum equatorial insolation^{23,24}, bi-hemisphere maximum insolation^{22,27} and bi-hemisphere maximum meridional insolation gradient¹⁹, and the cross-wavelet spectra between them is performed. The code for continuous wavelet transform and cross-wavelet spectra is available for download at <https://grinsted.github.io/wavelet-coherence/>, the related calculation and description can be found in the previous publications^{47,48}. In the cross-wavelet spectra, arrows pointing to the right indicate that the half-precession cycle is in-phase with the insolation index, suggesting a positive correlation. Arrows pointing to the left represent an anti-phase relationship, indicating a negative correlation. When the arrows point upward, it indicates that the half-precession cycle lags the insolation index by 2.5 ka (a quarter of the half-precession cycle). Conversely, downward-pointing arrows indicate a lag of 7.5 ka (three-

quarters of the half-precession cycle). The solution of ref. 40 is used to calculate the insolation data.

Data availability

Source data are provided with this paper. The data generated in this study have been deposited in the Figshare repository (<https://doi.org/10.6084/m9.figshare.27613614>)⁴⁹.

Code availability

The code for LOVECLIM1.3 is available at www.climate.be/loveclim. The Acycle v2.8 software can be obtained at: <https://acycle.org/>. The code for continuous wavelet transform and cross-wavelet spectra is available for download at <https://grinsted.github.io/wavelet-coherence/>.

References

1. Cane, M. A. A role for the tropical Pacific. *Science* **282**, 59–61 (1998).
2. Lau, K. M. & Yang, S. Climatology and interannual variability of the Southeast Asian summer monsoon. *Adv. Atmos. Sci.* **14**, 141–162 (1997).
3. Trenberth, K. E. et al. Progress during TOGA in understanding and modeling global teleconnections associated with tropical sea surface temperatures. *J. Geophys. Res.: Oceans* **103**, 14291–14324 (1998).
4. Fasullo, J. & Webster, P. J. Warm pool SST variability in relation to the surface energy balance. *J. Clim.* **12**, 1292–1305 (1999).
5. Xie, S. P. et al. Decadal shift in El Niño influences on Indo–western Pacific and East Asian climate in the 1970s. *J. Clim.* **23**, 3352–3368 (2010).
6. Yun, K. S. et al. Increasing ENSO–rainfall variability due to changes in future tropical temperature–rainfall relationship. *Commun. Earth Environ.* **2**, 43 (2021).
7. Khider, D., Jackson, C. S. & Stott, L. D. Assessing millennial-scale variability during the Holocene: A perspective from the western tropical Pacific. *Paleoceanography* **29**, 143–159 (2014).
8. Tachikawa, K., Timmermann, A., Vidal, L., Sonzogni, C. & Timm, O. E. CO₂ radiative forcing and Intertropical Convergence Zone influences on western Pacific warm pool climate over the past 400 ka. *Quat. Sci. Rev.* **86**, 24–34 (2014).
9. Raddatz, J., Nürnberg, D., Tiedemann, R. & Rippert, N. Southeastern marginal West Pacific Warm Pool sea-surface and thermocline dynamics during the Pleistocene (2.5–0.5 Ma). *Palaeogeogr. Palaeoclimatol. Palaeoecol.* **471**, 144–156 (2017).
10. de Garidel-Thoron, T., Rosenthal, Y., Bassinot, F. & Beaufort, L. Stable sea surface temperatures in the western Pacific warm pool over the past 1.75 million years. *Nature* **433**, 294–298 (2005).
11. Medina-Elizalde, M. & Lea, D. W. The mid-Pleistocene transition in the tropical Pacific. *Science* **310**, 1009–1012 (2005).
12. Hollstein, M. et al. Variations in Western Pacific Warm Pool surface and thermocline conditions over the past 110,000 years: Forcing mechanisms and implications for the glacial Walker circulation. *Quat. Sci. Rev.* **201**, 429–445 (2018).
13. Hollstein, M. et al. The impact of astronomical forcing on surface and thermocline variability within the Western Pacific Warm Pool over the past 160 kyr. *Paleoceanogr. Palaeoclimatol.* **35**, e2019PA003832 (2020).
14. Zhang, S. et al. Precession cycles of the El Niño/Southern oscillation-like system controlled by Pacific upper-ocean stratification. *Commun. Earth Environ.* **2**, 1–10 (2021).
15. Jian, Z. M. et al. Warm pool ocean heat content regulates ocean–continent moisture transport. *Nature* **612**, 92–99 (2022).
16. Lo, L. et al. Orbital control on the thermocline structure during the past 568 kyr in the Solomon Sea, southwest equatorial Pacific. *Quat. Sci. Rev.* **295**, 107756 (2022).
17. Sagawa, T., Okamura, K. & Murayama, M. Orbital-scale thermocline temperature variability in the western equatorial Pacific during the last 370 kyr. *Palaeogeogr., Palaeoclimatol., Palaeoecol.* **608**, 111285 (2022).

18. Lambert, J. E. et al. Obliquity-driven subtropical forcing of the thermocline after 240 ka in the southern sector of the Western Pacific Warm Pool. *Palaeogeogr., Palaeoclimatol., Palaeoecol.* **621**, 111578 (2023).
19. Jian, Z. M. et al. Half-precessional cycle of thermocline temperature in the western equatorial Pacific and its bihemispheric dynamics. *Proc. Natl Acad. Sci.* **117**, 7044–7051 (2020).
20. Hinnov, L. A., Schulz, M. & Yiou, P. Interhemispheric space-time attributes of the Dansgaard–Oeschger oscillations between 100 and 0 ka. *Quat. Sci. Rev.* **21**, 1213–1228 (2002).
21. Le Treut, H. & Ghil, M. Orbital forcing, climatic interactions, and glaciation cycles. *J. Geophys. Res.: Oceans* **88**, 5167–5190 (1983).
22. Rutherford, S. & D'Hondt, S. Early onset and tropical forcing of 100,000-year Pleistocene glacial cycles. *Nature* **408**, 72–75 (2000).
23. Berger, A. & Loutre, M. F. Intertropical latitudes and precessional and half-precessional cycles. *Science* **278**, 1476–1478 (1997).
24. Berger, A., Loutre, M. F. & Mélice, J. L. Equatorial insolation: from precession harmonics to eccentricity frequencies. *Clim. Past* **2**, 131–136 (2006).
25. Short, D. A., Mengel, J. G., Crowley, T. J., Hyde, W. T. & North, G. R. Filtering of Milankovitch cycles by Earth's geography. *Quat. Res.* **35**, 157–173 (1991).
26. Wu, Z. P., Yin, Q. Z., Guo, Z. T. & Berger, A. Hemisphere differences in response of sea surface temperature and sea ice to precession and obliquity. *Glob. Planet. Change* **192**, 103223 (2020).
27. Guo, Z. T., Zhou, X. & Wu, H. B. Glacial-interglacial water cycle, global monsoon and atmospheric methane changes. *Clim. Dyn.* **39**, 1073–1092 (2012).
28. Berger, A. Long-term variations of caloric insolation resulting from the Earth's orbital elements. *Quat. Res.* **9**, 139–167 (1978).
29. Izumo, T., Lengaigne, M., Vialard, J., Suresh, I. & Planton, Y. On the physical interpretation of the lead relation between Warm Water Volume and the El Niño Southern Oscillation. *Clim. Dyn.* **52**, 2923–2942 (2019).
30. Turney, C. S. et al. Millennial and orbital variations of El Niño/Southern Oscillation and high-latitude climate in the last glacial period. *Nature* **428**, 306–310 (2004).
31. Sun, J. M. & Huang, X. G. Half-precessional cycles recorded in Chinese loess: response to low-latitude insolation forcing during the Last Interglaciation. *Quat. Sci. Rev.* **25**, 1065–1072 (2006).
32. Wang, Y. et al. Tropical forcing orbital-scale precipitation variations revealed by a maar lake record in South China. *Clim. Dyn.* **58**, 2269–2280 (2022).
33. Guo, Z. T., Berger, A., Yin, Q. Z. & Qin, L. Strong asymmetry of hemispheric climates during MIS-13 inferred from correlating China loess and Antarctica ice records. *Clim. Past* **5**, 21–31 (2009).
34. Sun, Y. B. et al. Astronomical and glacial forcing of East Asian summer monsoon variability. *Quat. Sci. Rev.* **115**, 132–142 (2015).
35. Beck, J. W. et al. A 550,000-year record of East Asian monsoon rainfall from ¹⁰Be in loess. *Science* **360**, 877–881 (2018).
36. Bolliet, T. et al. Mindanao Dome variability over the last 160 kyr: Episodic glacial cooling of the West Pacific Warm Pool. *Paleoceanography* **26**, PA1208 (2011).
37. Lisiecki, L. E. & Raymo, M. E. A Pliocene–Pleistocene stack of 57 globally distributed benthic $\delta^{18}\text{O}$ records. *Paleoceanography* **20**, PA1003 (2005).
38. Goosse, H. et al. Description of the Earth system model of intermediate complexity LOVECLIM version 1.2. *Geosci. Model Dev.* **3**, 603–633 (2010).
39. Yin, Q. Z., Wu, Z. P., Berger, A., Goosse, H. & Hodell, D. Insolation triggered abrupt weakening of Atlantic circulation at the end of interglacials. *Science* **373**, 1035–1040 (2021).
40. Berger, A. & Loutre, M. F. Insolation values for the climate of the last 10 million years. *Quat. Sci. Rev.* **10**, 297–317 (1991).
41. Lüthi, D. et al. High-resolution carbon dioxide concentration record 650,000–800,000 years before present. *Nature* **453**, 379–382 (2008).
42. Louergue, L. et al. Orbital and millennial-scale features of atmospheric CH₄ over the past 800,000 years. *Nature* **453**, 383–386 (2008).
43. Schilt, A. et al. Glacial-interglacial and millennial-scale variations in the atmospheric nitrous oxide concentration during the last 800,000 years. *Quat. Sci. Rev.* **29**, 182–192 (2010).
44. Ganopolski, A. & Calov, R. The role of orbital forcing, carbon dioxide and regolith in 100 kyr glacial cycles. *Clim. Past* **7**, 1415–1425 (2011).
45. Wu, Z. P., Yin, Q. Z., Ganopolski, A., Berger, A. & Guo, Z. T. Effect of Hudson Bay closure on global and regional climate under different astronomical configurations. *Glob. Planet. Change* **222**, 104040 (2023).
46. Li, M. S., Hinnov, L. & Kump, L. Acycle: Time-series analysis software for paleoclimate research and education. *Comput. Geosci.* **127**, 12–22 (2019).
47. Melice, J. L. & Servain, J. The tropical Atlantic meridional SST gradient index and its relationships with the SOI, NAO and Southern Ocean. *Clim. Dyn.* **20**, 447–464 (2003).
48. Grinsted, A., Moore, J. C. & Jevrejeva, S. Application of the cross wavelet transform and wavelet coherence to geophysical time series. *Nonlinear Proc. Geophys.* **11**, 561–566 (2004).
49. Wu, Z. P., Yin, Q. Z., Berger, A., & Guo, Z. T. Supporting data for “Forcing mechanisms of the half-precession cycle in the western equatorial Pacific temperature”. Available online at: <https://doi.org/10.6084/m9.figshare.27613614> (2025).

Acknowledgements

This work is supported by the Fonds de la Recherche Scientifique-FNRS (F.R.S.-FNRS) under grants n° T.0246.23 and n° T.W019.23 through funding to Q.Y. and the National Natural Science Foundation of China (Grant No. 42488201) through funding to Z.G. Q.Y. is Senior Research Associate and Z.W. is Postdoctoral Researcher of F.R.S.-FNRS. Computational resources have been provided by the supercomputing facilities of the Université catholique de Louvain (CISM/UCL) and the Consortium des Équipements de Calcul Intensif en Fédération Wallonie Bruxelles (CÉCI) funded by the F.R.S.-FNRS under convention 2.5020.11 and by the Walloon Region. We are grateful to Dr. Martina Hollstein, Prof. Yue Wang and Prof. Li Lo for sharing their data.

Author contributions

Q.Y. designed the study. Z.W. and Q.Y. performed model simulations, interpreted model and proxy data, and wrote the first draft of the manuscript with contributions from A.B. and Z.G. to the final version.

Competing interests

The authors declare no competing interests.

Additional information

Supplementary information The online version contains supplementary material available at <https://doi.org/10.1038/s41467-025-57076-2>.

Correspondence and requests for materials should be addressed to Zhipeng Wu or Qiuzhen Yin.

Peer review information *Nature Communications* thanks the anonymous reviewers for their contribution to the peer review of this work. A peer review file is available.

Reprints and permissions information is available at <http://www.nature.com/reprints>

Publisher's note Springer Nature remains neutral with regard to jurisdictional claims in published maps and institutional affiliations.

Open Access This article is licensed under a Creative Commons Attribution-NonCommercial-NoDerivatives 4.0 International License, which permits any non-commercial use, sharing, distribution and reproduction in any medium or format, as long as you give appropriate credit to the original author(s) and the source, provide a link to the Creative Commons licence, and indicate if you modified the licensed material. You do not have permission under this licence to share adapted material derived from this article or parts of it. The images or other third party material in this article are included in the article's Creative Commons licence, unless indicated otherwise in a credit line to the material. If material is not included in the article's Creative Commons licence and your intended use is not permitted by statutory regulation or exceeds the permitted use, you will need to obtain permission directly from the copyright holder. To view a copy of this licence, visit <http://creativecommons.org/licenses/by-nc-nd/4.0/>.

© The Author(s) 2025